

# Evaluation of fluorophores for optimal performance in localization-based super-resolution imaging

Graham T Dempsey<sup>1,6</sup>, Joshua C Vaughan<sup>2,3,6</sup>, Kok Hao Chen<sup>3,6</sup>, Mark Bates<sup>4</sup> & Xiaowei Zhuang<sup>2,3,5</sup>

One approach to super-resolution fluorescence imaging uses sequential activation and localization of individual fluorophores to achieve high spatial resolution. Essential to this technique is the choice of fluorescent probes; the properties of the probes, including photons per switching event, on-off duty cycle, photostability and number of switching cycles, largely dictate the quality of super-resolution images. Although many probes have been reported, a systematic characterization of the properties of these probes and their impact on super-resolution image quality has been described in only a few cases. Here we quantitatively characterized the switching properties of 26 organic dyes and directly related these properties to the quality of super-resolution images. This analysis provides guidelines for characterization of super-resolution probes and a resource for selecting probes based on performance. Our evaluation identified several photoswitchable dyes with good to excellent performance in four independent spectral ranges, with which we demonstrated low-cross-talk, four-color super-resolution imaging.

The spatial resolution limit of light microscopy imposed by diffraction has recently been overcome by super-resolution fluorescence imaging methods<sup>1,2</sup>. Among these methods, stochastic optical reconstruction microscopy (STORM)<sup>3</sup> and (fluorescence) photoactivated localization microscopy<sup>4,5</sup> can be used to achieve sub-diffraction-limit resolution by sequentially imaging and localizing individual fluorophores that label the target structure. The basic concept of single-molecule-localization-based super-resolution imaging entails (i) sparse activation of an optically resolvable subset of fluorophores, (ii) determination of the positions of these fluorophores with sub-diffraction-limit precision and (iii) repeating this process to allow stochastically different subsets of fluorophores to be turned on and localized each time (Fig. 1a). An image with sub-diffraction-limit resolution can then be reconstructed from the positions of the many activated molecules.

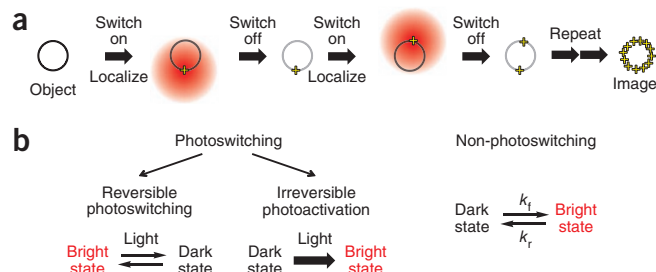
As stated in the original STORM paper<sup>3</sup>, “we demonstrate the concept of STORM using the cyanine switch, but in principle any suitable optically switched fluorophore could be used” and “the

STORM concept is also applicable to other photoswitchable fluorophores and fluorescent proteins.” Indeed, a variety of fluorescent probes have been used for localization-based super-resolution imaging, including organic dyes<sup>3,6–21</sup>, fluorescent proteins<sup>4,5,22,23</sup> and quantum dots<sup>24</sup>. In the simplest imaging mode, continuous illumination of a single dye (for example, Alexa Fluor 647) with a single laser wavelength can generate high-quality STORM images, where the laser accomplishes all three tasks of activating the dye to the fluorescent state, exciting fluorescence from the dye and switching it off to the dark state<sup>14</sup>. As Alexa Fluor 647, a variety of commonly used organic dyes spanning a broad spectrum of colors can transition between fluorescent and dark states and have been used for super-resolution imaging<sup>8,10,11,14–16</sup>. Depending on the fluorescent probes used, this imaging method has also been referred to by several other names (for example, direct (d)STORM<sup>11,15</sup>), which use the same fundamental imaging principle as STORM, a technique generally applicable to photoswitchable probes.

The photoswitchable probes can be largely divided into two categories (Fig. 1b): (i) reversibly switchable probes that can be converted between fluorescent (on) and dark (off) states multiple times upon excitation by light either of the same or different wavelengths and (ii) irreversibly activatable probes that exist initially in a dark state and can be activated by light to a fluorescent state. Examples in the first category include photoswitchable cyanine, rhodamine and oxazine dyes<sup>3,6,7,10,15,16</sup> and photoswitchable fluorescent proteins such as Dronpa<sup>25</sup>, Dreiklang<sup>26</sup> and reversibly switchable enhanced GFP (rsEGFP)<sup>27</sup>. Examples in the second category include dark-to-bright fluorescent proteins such as photoactivatable (PA)-GFP<sup>28</sup> and PA-mCherry<sup>29</sup>, color-converting fluorescent proteins such as photoswitchable CFP<sup>30</sup>, EosFP<sup>31,32</sup> and Dendra2 (ref. 33), and push-pull fluorogen dyes<sup>18</sup>, although in some cases, photoactivatable fluorescent proteins may also undergo reversible photoswitching once photoactivated. In addition to photoswitchable fluorophores, probes that can be turned on and off by non-optical means such as reversible ligand binding<sup>34</sup> or by fluorescence quenchers<sup>19</sup> have also been used for localization-based super-resolution fluorescence microscopy (Fig. 1b).

<sup>1</sup>Graduate program in Biophysics, Harvard University, Cambridge, Massachusetts, USA. <sup>2</sup>Howard Hughes Medical Institute, Harvard University, Cambridge, Massachusetts, USA. <sup>3</sup>Department of Chemistry and Chemical Biology, Harvard University, Cambridge, Massachusetts, USA. <sup>4</sup>School of Engineering and Applied Sciences, Harvard University, Cambridge, Massachusetts, USA. <sup>5</sup>Department of Physics, Harvard University, Cambridge, Massachusetts, USA. <sup>6</sup>These authors contributed equally to this work. Correspondence should be addressed to X.Z. (zhuang@chemistry.harvard.edu).

**Figure 1** | Principle of single-molecule localization-based super-resolution imaging and modes of switching used for this imaging method. **(a)** A structure (here a ring-like object) smaller than the diffraction-limited resolution is densely labeled with switchable fluorophores. When the fluorophores are imaged simultaneously, the spatial features of the structure are obscured by the overlapping fluorescence images of individual molecules. However, the positions of individual molecules may be determined with high precision when the molecules are activated and imaged sequentially (fluorescent image indicated as a red circle whose center position is marked as a yellow '+'). By repeatedly activating and localizing different molecules labeling the structure, the sub-diffraction-limited spatial features can be resolved. **(b)** This principle can be performed by using photoswitching or non-photoswitching modes. The first mode includes reversibly switchable or irreversibly activatable fluorophores. The non-photoswitching mode can be achieved, for example, through reversible binding of fluorescently labeled ligands or chemical quenching of fluorescence.



Here we focused on reversibly photoswitchable dyes, which include the majority of organic dyes used for localization-based super-resolution imaging. Two properties of switchable probes crucial to super-resolution image quality are (i) the number of photons detected per switching event and (ii) the on-off duty cycle (or the fraction of time a fluorophore spends in the on state)<sup>2,35</sup>. Switching events with a high photon yield are desired for accurate determination of a probe's position owing to the approximate inverse-square-root dependence of the localization precision on the number of detected photons<sup>36,37</sup>. Hence, the photon number limits the obtainable optical resolution. A low duty cycle is generally beneficial because the maximum number of fluorophores that can be localized in a diffraction-limited area is inversely proportional to the duty cycle (a fluorophore with a duty cycle of  $1/N$  typically allows less than  $N$  molecules to be localized in a diffraction-limited area). This maximum fluorophore density in turn limits the image resolution according to the Nyquist sampling criterion<sup>38</sup>, which equates the maximal achievable resolution to twice the average distance between neighboring probes. We illustrated the importance of the number of photons per switching event and the duty cycle for three hypothetical cases: (i) a fluorophore with a high photon yield per switching event and a low duty cycle provides both high localization precision and high localization density, and thus can be used to resolve small structures such as the hollow ring structure shown in **Figure 2a**; (ii) a fluorophore with a low photon yield can only be localized with low precision and consequently blurs out the hollowness of the ring structure (**Fig. 2b**); (iii) a fluorophore with a high on-off duty cycle limits the density of probes that can be localized in a diffraction-limited area, which also obscures the hollow ring structure owing to an insufficient number of localizations (**Fig. 2c**).

Although many fluorophores have been used for STORM, relatively few have been quantitatively and systematically characterized in terms of photon yield and on-off duty cycle, let alone other important properties that influence image quality or acquisition speed, such as the photostability, the total number of photoswitching cycles and the ability to control the fluorophore activation rate by a light source independent from the imaging light. Furthermore, the imaging buffer conditions can strongly impact the fluorophore switching properties and the resulting image quality<sup>12,39</sup>, and yet the roles of different buffer components are not well understood for many fluorophores. Consequently, the incomplete quantitative information on the photoswitching properties makes it difficult to systematically

choose the optimal fluorophores and imaging conditions for attaining high-quality super-resolution images.

In this Analysis, we addressed this problem by evaluating 26 commercially available fluorophores and their suitability for STORM imaging. We focused on organic dyes that can reversibly switch between on and off states before photobleaching. We provided single-molecule characterization of the number of photons detected per switching event, the on-off duty cycle, the photostability and the sensitivity to photoactivation by violet light for all dyes, and corroborated these measurements with STORM images in all cases to demonstrate the impact of a dye's switching properties on image quality. We also explored the importance of buffer conditions on dye performance. Our characterization provides a resource of quantitative information about each fluorophore's switching properties to facilitate fluorophore selection for STORM applications as well as a set of guidelines for evaluating the fitness of fluorophores for STORM in general. We also identified several high-quality switchable dyes in different spectral ranges, which we used to demonstrate low cross-talk, four-color super-resolution imaging.

## RESULTS

### Investigated dyes

We evaluated 26 organic dyes spanning the visible and near infrared (NIR) spectral range. These dyes include blue-absorbing (Atto 488, Alexa Fluor 488, Atto 520, fluorescein, FITC and Cy2), yellow-absorbing (Cy3B, Alexa Fluor 568, TAMRA, Cy3, Cy3.5 and Atto 565), red-absorbing (Alexa Fluor 647, Cy5, Atto 647, Atto 647N, Dyomics 654, Atto 655, Atto 680 and Cy5.5) and NIR-absorbing (DyLight 750, Cy7, Alexa Fluor 750, Atto 740, Alexa Fluor 790 and IRDye 800CW) fluorophores. They can be categorized structurally as cyanines (Cy2, Cy3, Cy3B, Cy3.5, Cy5, Alexa Fluor 647, Dyomics 654, Cy5.5, Cy7, DyLight 750, Alexa Fluor 750, Alexa Fluor 790 and IRDye 800CW), rhodamines (Alexa Fluor 488, Atto 488, Atto 520, TAMRA, Atto 565 and Alexa Fluor 568), oxazines (Atto 655 and Atto 680), carbopyronines (Atto 647N, Atto 647 and Atto 740) and fluoresceins (FITC and fluorescein).

Previously, STORM imaging has been performed either with activator-reporter dye pairs<sup>3,6,12,14,40,41</sup>, in which 'activator' molecules are used to enhance the activation rate of the photo-switchable 'reporter' molecules or photoswitchable reporters alone<sup>8,10,11,14–16</sup>. As the intrinsic properties of the photoswitchable reporters limit the STORM imaging performance in both cases in a similar manner, we characterized these properties in the reporter-alone configuration.

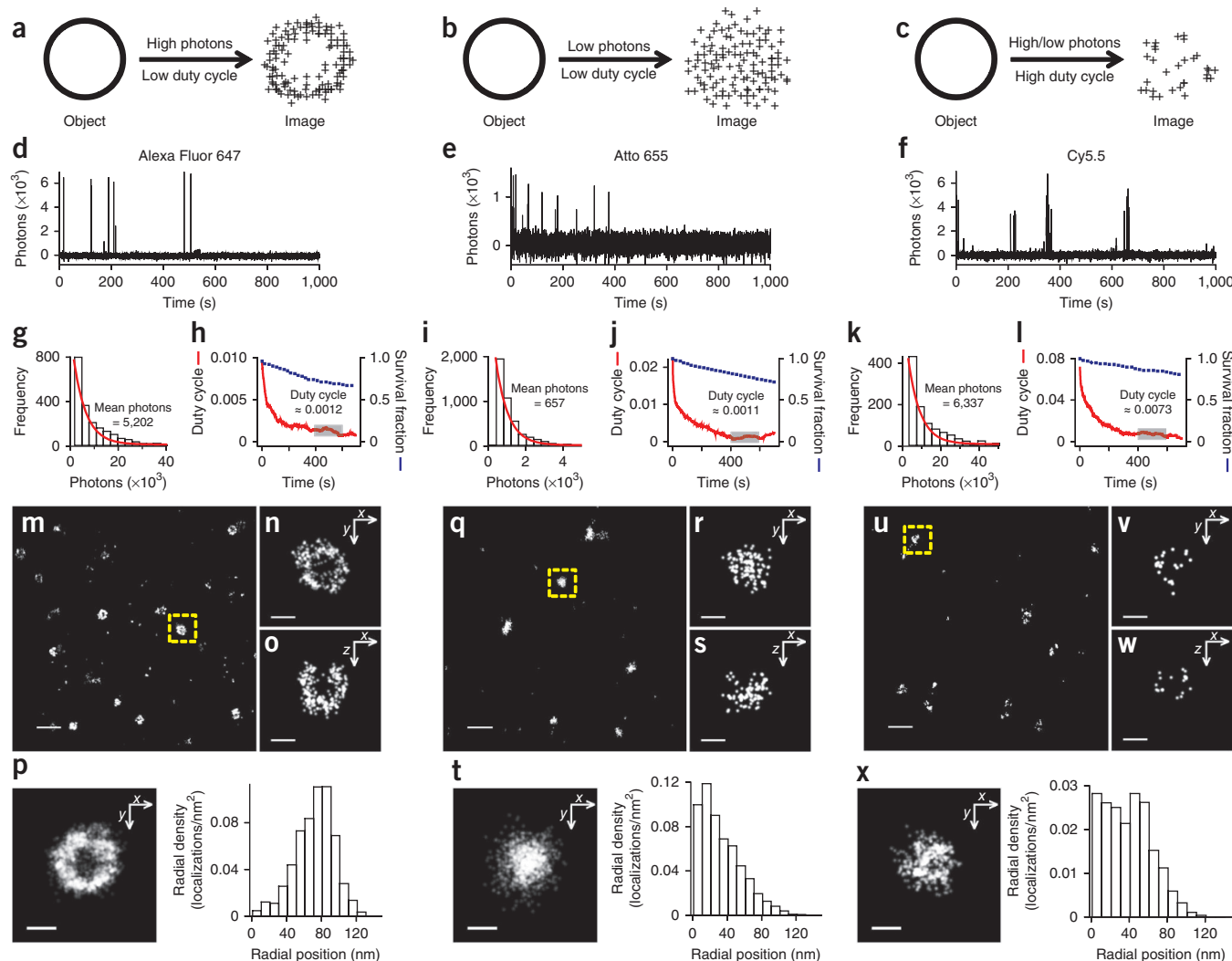


**Figure 2 | Quantitative probe characterization for STORM imaging.** (a–c) The effect of number of detected photons per on-switching event and the on-off duty cycle (fraction of time in the on state) on STORM image quality for an example structure (a ring-like object). A fluorophore with high photon number and low duty cycle produces a hollow, ring-like image with high localization precision and sufficient density (a). A fluorophore with low photon number and low duty cycle maintains a large number of localizations but suffers reduced localization accuracy, obscuring the ring-like structure (b). A fluorophore with high on-off duty cycle requires reduction in the density of fluorescent probes to allow single-molecule localization, which in turn reduces the number of localizations and adversely affects the overall resolution (c). (d–f) Single-molecule fluorescence time traces measured in the presence of  $\beta$ ME and an oxygen-scavenging system for (d) Alexa Fluor 647, (e) Atto 655 and (f) Cy5.5. These dyes represent the scenarios in a–c. (g–l) From traces such as those shown in d–f, the number of detected photons was determined for each switching event, and a histogram was constructed (g–i) from many events from hundreds of molecules (g,i,k). The indicated mean value was derived from the single exponential fit of the distribution (red curves). The on-off duty cycle value was calculated for each dye and plotted versus time (red curve; h,j,l) to show how each value begins high when most molecules are in the fluorescent state and reaches a quasi-equilibrium later. Reported values are the average duty cycle measured between 400–600 s (gray box). The fraction of molecules that survived photobleaching was plotted together with the duty cycle (blue squares). (m–x) Images of CCPs in three dimensions using Alexa Fluor 647 (m–p), Atto 655 (q–t) and Cy5.5 (u–x). Shown are 2D projection images (m,q,u) and, for CCPs marked by yellow dashed boxes, x–y (n,r,v) and x–z (o,s,w) cross-sections. Composite x–y cross-sections for ten CCPs aligned to their respective centers of mass are shown along with the radial density distributions of localizations derived from the composite x–y cross-sections (p,t,x). Scale bars, 500 nm (m,q,u) and 100 nm (n–p,r–t,v–x).

### Method of photoswitchable probe characterization

We characterized the switching properties using dye-labeled proteins that were adsorbed to coverglass and illuminated with light at 488 nm, 561 nm, 647 nm or 752 nm, to excite blue, yellow, red or NIR dyes, respectively. Under these conditions, many fluorophores reversibly transition between on and off states with a characteristic duty cycle and number of emitted photons per switching event. Although it is often convenient to use an additional ‘activation laser’ to increase the on-switching rate and hence speed up the imaging process, the on-off duty cycle determined in the absence of the

activation laser represents the lowest achievable duty cycle for a dye and thus sets the resolution limit based on the Nyquist criterion. The number of detected photons per switching event is typically the same independent of whether an additional activation light is used.

For each dye, we determined four switching properties: (i) number of photons detected per switching event, (ii) on-off duty cycle, (iii) survival fraction and (iv) number of switching cycles. We recorded the number of photons detected in each switching event for many molecules, from which we constructed a photon-number histogram and determined the mean value.

**Table 1** | Summary of switching properties of the 26 dyes tested in this study

Dye	Excitation maximum (nm) <sup>a</sup>	Emission maximum (nm) <sup>a</sup>	Extinction (M <sup>-1</sup> cm <sup>-1</sup> ) <sup>b</sup>	Quantum yield <sup>c</sup>	Detected photons per switching event		Equilibrium on-off duty cycle (400–600 s)		Survival fraction after illumination for 400 s		Number of switching cycles (mean)	
					MEA	βME	MEA	βME	MEA	βME	MEA	βME
Blue-absorbing												
Atto 488	501	523	90,000	0.8	1,341	1,110	0.00065	0.0022	0.98	0.99	11	49
Alexa Fluor 488	495	519	71,000	0.92	1,193	427	0.00055	0.0017	0.94	1	16	139
Atto 520	516	538	110,000	0.9	1,231	868	0.0015	0.00061	0.92	0.86	9	17
Fluorescein	494	518	70,000	0.79	1,493	776	0.00032	0.00034	0.51	0.83	4	15
FITC	494	518	70,000	0.8	639	1,086	0.00041	0.00031	0.75	0.9	17	16
Cy2	489	506	150,000	0.12	6,241	4,583	0.00012	0.00045	0.12	0.19	0.4	0.7
Yellow-absorbing												
Cy3B	559	570	130,000	0.67	1,365	2,057	0.0003	0.0004	1	0.89	8	5
Alexa Fluor 568	578	603	91,300	0.69	2,826	1,686	0.00058	0.0027	0.58	0.99	7	52
TAMRA	546	575	90,430	0.2	4,884	2,025	0.0017	0.0049	0.85	0.99	10	59
Cy3	550	570	150,000	0.15	11,022	8,158	0.0001	0.0003	0.17	0.55	0.5	1.6
Cy3.5	581	596	150,000	0.15	4,968	8,028	0.0017	0.0005	0.89	0.61	5.7	3.3
Atto 565	563	592	120,000	0.9	19,714	13,294	0.00058	0.00037	0.17	0.26	4	5
Red-absorbing												
Alexa Fluor 647	650	665	239,000	0.33	3,823	5,202	0.0005	0.0012	0.83	0.73	14	26
Cy5	649	670	250,000	0.28	4,254	5,873	0.0004	0.0007	0.75	0.83	10	17
Atto 647	645	669	120,000	0.2	1,526	944	0.0021	0.0016	0.46	0.84	10	24
Atto 647N	644	669	150,000	0.65	3,254	4,433	0.0012	0.0035	0.24	0.65	9	39
Dyomics 654	654	675	220,000	–	3,653	3,014	0.0011	0.0018	0.79	0.64	20	19
Atto 655	663	684	125,000	0.3	1,105	657	0.0006	0.0011	0.65	0.78	17	22
Atto 680	680	700	125,000	0.3	1,656	987	0.0019	0.0024	0.65	0.91	8	27
Cy5.5	675	694	250,000	0.28	5,831	6,337	0.0069	0.0073	0.87	0.85	16	25
NIR-absorbing												
DyLight 750	752	778	220,000	–	712	749	0.0006	0.0002	0.55	0.58	5	6
Cy7	747	776	200,000	0.28	852	997	0.0003	0.0004	0.48	0.49	5	2.6
Alexa Fluor 750	749	775	240,000	0.12	437	703	0.00006	0.0001	0.36	0.68	1.5	6
Atto 740	740	764	120,000	0.1	779	463	0.00047	0.0014	0.31	0.96	3	14
Alexa Fluor 790	785	810	260,000	–	591	740	0.00049	0.0014	0.54	0.62	5	2.7
IRDye 800 CW	778	794	240,000	–	2,753	2,540	0.0018	0.038	0.6	1	3	127

Excitation wavelength, dichroic mirrors and emission filters used for characterization and imaging for each spectral range were 488 nm, T495LP (Chroma) and ET535/50m (Chroma) for blue-absorbing dyes; 561 nm, Di01-R561 (Semrock) and FF01-617/73-25 (Semrock) for yellow-absorbing dyes; 647 nm, Z660DCXRU (Chroma) and ET700/75m (Chroma) for red-absorbing dyes; 752 nm, Q770DCXR (Chroma) and HQ800/60m (Chroma) for NIR-absorbing dyes, respectively. Dye-switching properties are reported in the presence of GLOX and 10 mM MEA as well as GLOX and 140 mM βME.

<sup>a</sup>Excitation and emission peak wavelengths from dye spectra. <sup>b</sup>Extinction coefficients from the dye manufacturers. <sup>c</sup>Quantum yields from either the dye manufacturer when known or from the McNamara 2007 fluorophore data tables. –, quantum yield values not available from dye manufacturer or McNamara data tables.

We measured the on-off duty cycle as the fraction of time spent in the on state averaged over many molecules. Because the molecules were originally in the on state and a certain illumination time is required for them to reach a quasi-equilibrium between the on and off states, we used a sliding window of 100 s to monitor changes in the on-off duty cycle as a function of exposure time. The duty cycle value during the time window 400–600 s was used to represent the characteristic, equilibrium duty cycle because the dyes typically achieved quasi-equilibrium between on and off states by this point. As some dyes switched for a limited number of cycles before photobleaching, a substantial fraction of molecules may be photobleached by the time the on-off equilibrium is reached. We therefore also characterized the survival fraction of unbleached molecules as a function of illumination time. This quantity can be used together with the time-dependent duty cycle value to determine what degree of photobleaching has occurred before achieving a sufficiently low density to resolve single molecules. Finally, we determined for each molecule the number of switching cycles during the data

acquisition time, which represents a lower bound value, given that some molecules did not photobleach before the end of the observation period.

We correlated the above properties with the quality of STORM images for each dye by recording images of different cellular structures, including microtubules, which have a linear (or cylindrical) morphology, and clathrin-coated pits (CCPs), which have a spherical morphology. Because the switching performance and photostability of many dyes are enhanced by the presence of a primary thiol and/or a low oxygen environment, we performed experiments in the presence of an enzymatic oxygen-scavenging system and a primary thiol, either β-mercaptoethanol (βME) or mercaptoethylamine (MEA), unless otherwise indicated.

In **Figure 2d–l** we illustrate our method of dye characterization, using Alexa Fluor 647, Atto 655 and Cy5.5 as representative examples. We show examples of single-molecule fluorescence time traces (**Fig. 2d–f** and **Supplementary Fig. 1**), histograms of photon number distributions (**Fig. 2g,i,k**) and duty cycle plots along with the corresponding survival fractions (**Fig. 2h,j,l**).



The dyes exhibited three distinct switching behaviors: high photon yield per switching event and low duty cycle (Alexa Fluor 647), low photon yield and low duty cycle (Atto 655), and high photon yield and high duty cycle (Cy5.5).

### Photon number and duty cycle

To analyze the importance of photon number and duty cycle, we recorded three-dimensional (3D) STORM images of CCPs, which provided an excellent metric for assessing a dye's performance because of their small size (~100–200 nm in diameter) and the requirement for high spatial resolution to reveal their hollow, spherical shell-like structure. We collected 3D STORM images using astigmatism imaging, an easy-to-implement 3D super-resolution imaging approach<sup>40</sup>. When imaging Alexa Fluor 647-labeled CCPs, the hollow shape of the pit was clearly resolved (**Fig. 2m–p**) owing to the high photon yield of individual switching events (~5,000 photons; **Fig. 2g**) and low on-off duty cycle (~0.001, **Fig. 2h**). The *x–y* and *x–z* cross-sections taken from the midplanes of an example CCP revealed the expected cup-like shape of the pit (**Fig. 2n,o**). The superposition of *x–y* cross-sections of multiple CCPs showed the expected hollow, ring-like structure (**Fig. 2p**).

In contrast to Alexa Fluor 647, the low photon yield of Atto 655 (~660 photons per switching event; **Fig. 2i**), and the resulting low localization precision, blurred the CCP image substantially such that its hollowness was no longer apparent (**Fig. 2q–t**), despite the fact that the duty cycle of Atto 655 (~0.001, **Fig. 2j**) was comparable to that of Alexa Fluor 647. In a different manner, the high duty cycle of Cy5.5 (~0.007, **Fig. 2l**) also negatively impacted the quality of the CCP images (**Fig. 2u–x**). Because of the large fraction of time each dye spent in the fluorescent state, a considerable reduction in labeling density (or photobleaching of molecules before imaging) was necessary to ensure single-molecule detection and localization. As a result, the sparse localization pattern no longer resolved the hollow morphology of the CCP, despite the high photon yield of Cy5.5 (~6,000 photons per switching event, **Fig. 2k**). These examples demonstrate that both high photon number and low duty cycle are essential to achieving high-resolution STORM images. In **Supplementary Figures 2–27** and **Table 1**, we show the wide range of photon number and duty cycle values of the 26 dyes.

### Photostability and number of switching cycles

The dyes also exhibited large variations in their survival fraction and number of switching cycles (**Supplementary Figs. 2–27** and **Table 1**). Although the three dyes analyzed in the experiments shown in **Figure 2** had comparably high survival fractions after the molecules reached an on-off equilibrium state (**Fig. 2h,j,l**), some dyes photobleached much more rapidly. For example, Cy2 showed little recovery to the on state after the initial switching off event, and by the time the duty cycle reached equilibrium, only a very small fraction of molecules survived. Consequently, we could not reconstruct a STORM image using Cy2 (**Supplementary Fig. 7**). An interesting example is Atto 565 (**Supplementary Fig. 13**). Despite having the highest photon yield per switching cycle among all the dyes screened, its relatively low survival fraction upon reaching on-off equilibrium led to overall lower quality STORM images compared to many other dyes with lower photon yields but higher survival fractions.

Related to the survival fraction is the number of switching cycles afforded by a fluorophore. Although it is desirable to have a single switching cycle for some applications, such as for counting molecules, in many cases, a large number of switching events is advantageous. Specifically, the detection of multiple switching events from the same fluorophore reduces the stochasticity of the localization error, and in the limit of many cycles, the mean localization positions converge with the true positions of the fluorophores (**Supplementary Fig. 28a**). This effect directly impacts the STORM image quality in that a dye with a low number of switching cycles often results in an image with more jagged and ill-defined spatial features because of localization errors, whereas a dye with a large number of switching cycles results in a smoother and more continuous image because of repetitive sampling of the same structure and thus lower noise in the final image (**Supplementary Fig. 28b**). For instance, dyes with relatively few switching cycles, such as Cy3, produced STORM images with sparse localization densities and overall poor quality regardless of whether the dyes have a high photon number and/or low on-off duty cycle (**Supplementary Fig. 11**). In contrast, fluorophores that exhibited a high number of switching cycles, such as Atto 488 (**Supplementary Fig. 2**), resulted in more continuous and better-defined microtubule or CCP structures, in spite of a relatively low photon yield.

### Sensitivity of fluorophores to violet-light activation

During acquisition of a STORM movie, the number of molecules present in a given frame decreases as the fluorophores are photobleached. This reduction, in turn, decreases the information content in a single frame and increases the number of frames

**Table 2** | Sensitivity to violet-light photoactivation

Dye		Sensitivity <sup>a</sup>
Blue-absorbing	Atto 488	+
	Alexa Fluor 488	+
	Atto 520	+
	Fluorescein	–
	FITC	–
	Cy2	–
Yellow-absorbing	Cy3B	+
	Alexa Fluor 568	+
	TAMRA	–
	Cy3	–
	Cy3.5	+
	Atto 565	+
Red-absorbing	Alexa Fluor 647	++
	Cy5	++
	Atto 647	+
	Atto 647N	+
	Dyomics 654	++
	Atto 655	+
	Atto 680	+
	Cy5.5	++
NIR-absorbing	Dylight 750	++
	Cy7	++
	Alexa Fluor 750	++
	Atto 740	+
	Alexa Fluor 790	++
	IRDye 800CW	++

<sup>a</sup>Fraction of single fluorescent molecules that activate after a 0.25 s pulse of 405 nm excitation light (10–30 W cm<sup>–2</sup>) relative to the total initial population was measured for each dye. Dyes were assigned a “–”, “+” or “++” if <3%, 3–25% or >25% were reactivated, respectively.

**Table 3** | Effect of buffer composition on photoswitching properties

Dye		Buffer condition			
		No GLOX or thiol	Thiol only	GLOX only	GLOX and thiol
Blue-absorbing	Atto 488	+	+	++	++
	Alexa Fluor 488	+	+	++	++
	Atto 520	+	+	++	++
	Fluorescein	–	+	+	+
	FITC	–	+	+	+
	Cy2	–	–	–	–
Yellow-absorbing	Cy3B	+	+	++	++
	Alexa Fluor 568	–	–	+	+
	TAMRA	–	–	–	+
	Cy3	–	–	+	+
	Cy3.5	–	–	+	+
	Atto 565	–	–	+	+
Red-absorbing	Alexa Fluor 647	–	+	–	++
	Cy5	–	+	–	++
	Atto 647	+	+	+	+
	Atto 647N	+	–	–	+
	Dyomics 654	–	+	–	++
	Atto 655	+	+	+	++
	Atto 680	+	+	++	++
	Cy5.5	–	–	–	+
	DyLight 750	–	+	–	++
NIR-absorbing	Cy7	–	+	–	++
	Alexa Fluor 750	–	+	–	+
	Atto 740	–	+	+	+
	Alexa Fluor 790	–	+	–	+
	IRDye 800CW	–	–	–	–

Cells were immunostained for microtubules using each of the dyes. The thiol used was MEA. Dyes were assigned a “–”, “+” or “++” if rapid bleaching (no image), low to moderate photoswitching (low to moderate quality image) or robust photoswitching (high quality image) was observed, respectively. Whereas lower image quality (+) was observed for Atto 647N and Alexa Fluor 750 in the ‘GLOX and thiol’ condition, reasonable image quality (++) was observed for these two dyes when  $\beta$ ME was used instead of MEA.

required to construct an image. The use of an ‘activation’ laser of a different wavelength from the excitation laser can increase the activation rate and thus reduce the image acquisition time. In the case of activator-reporter pairs, the activator molecules allow the reporter to be activated by using visible light of different colors<sup>6</sup>. When a photoswitchable reporter alone is used for STORM imaging, the activation rate is typically controlled by an ultraviolet or violet light<sup>10,20,39</sup>. We tested how the dyes responded to short-wavelength activation by switching a field of molecules to a stable dark state and then measuring the fraction of molecules that recovered following a pulse of violet (405 nm) light. Several red and NIR dyes showed appreciable recovery after 405-nm illumination, whereas even the most sensitive blue and yellow dyes showed modest recovery (Table 2).

### Dependence of switching properties on buffer composition

The switching properties of dyes can depend strongly on buffer composition. We tested the switching performance of all dyes under four different buffer conditions: (i) our standard buffers containing both an oxygen scavenging system (glucose oxidase with catalase (GLOX)) and a primary thiol ( $\beta$ ME or MEA), ‘GLOX and thiol’, (ii) a buffer with GLOX but no thiol, ‘GLOX only’, (iii) a buffer with a thiol (MEA) but no GLOX, ‘thiol only’ and (iv) a buffer with neither GLOX nor thiol, ‘no GLOX or thiol’. Nearly all of the tested dyes photobleached rapidly under the ‘no GLOX or thiol’ or ‘thiol only’ conditions, whereas several dyes

switched reasonably well in the ‘GLOX only’ condition (Atto 488, Alexa Fluor 488, Atto 520, Cy3B and Atto 680; Table 3 and Supplementary Figs. 29–30). With all 26 dyes we achieved equal or better imaging results when using buffers containing both GLOX and thiol (Table 3 and Supplementary Figs. 29–30).

To more concretely illustrate the effect of thiol or oxygen on dye switching, we quantitatively characterized the switching properties of Alexa Fluor 647, Atto 488 and Atto 655 under the four buffer conditions stated above (Supplementary Fig. 29). Consistent with previous observations, Alexa Fluor 647 required thiol for photoswitching, and the photon yield per switching cycle, photostability and number of switching cycles further increased when oxygen was removed by GLOX<sup>42–44</sup>. In contrast, Atto 488 switched well in the absence of thiol but performed best in buffer containing GLOX. In particular, the photostability of Atto 488 increased in the order of ‘no GLOX or thiol’ or ‘thiol only’ < ‘GLOX only’ < ‘GLOX and thiol’, and this order correlated well with STORM image quality. In the case of Atto 655, which has been previously proposed to switch well in the presence of a thiol under ambient (high) oxygen concentrations without the need of an oxygen-scavenger system<sup>15</sup>, we observed substantially better performance in the ‘GLOX and thiol’ condition and found that even the ‘GLOX only’ condition yielded better photostability and image quality than the ‘thiol only’ condition.

Different thiols can be used to facilitate switching of dyes. We quantitatively characterized all 26 dyes in both MEA (10 mM) and  $\beta$ ME (140 mM), where the chosen thiol concentrations were in the range of typical use reported previously<sup>6,12,39</sup>. In some cases, the switching behavior was rather sensitive to the thiol concentration, as illustrated by more detailed investigations of Atto 488, Cy3B, Alexa Fluor 647, Atto 655 and DyLight 750. We found that low to moderate concentrations of MEA enhanced the dye’s switching performance and STORM image quality (Table 3 and Supplementary Figs. 29 and 31), but high concentrations (100 mM) of MEA diminished either the number of switching cycles (Cy3B) or the number of photons per switching cycle (Atto 488 and Alexa Fluor 647) or both (DyLight 750 and Atto 655) (Supplementary Fig. 31). Optimal performance was achieved under relatively low MEA concentrations for these five dyes (1–10 mM, Supplementary Fig. 31), in contrast to the 50–200 mM concentrations previously recommended<sup>12,39</sup>.

Some dyes also behaved differently in the presence of different thiols. For instance, the duty cycles of Atto 488 and Alexa Fluor 647 were substantially lower in the presence of MEA than with  $\beta$ ME (Supplementary Figs. 2 and 14)<sup>12</sup>, whereas DyLight 750 showed the opposite trend (Supplementary Fig. 22). Notably, STORM images of good quality could be acquired with Atto 647N and Alexa Fluor 750 in the presence of  $\beta$ ME, whereas the survival fractions for both dyes were reduced to a nearly unusable level when using MEA (Supplementary Figs. 17 and 24).

These results emphasize the importance of buffer formulation in STORM imaging. We therefore recommend that buffer conditions be optimized for any given probe.

### Dependence of switching properties on light intensity

The imaging laser intensity is another adjustable parameter during STORM imaging. Often, we found the number of photons per switching cycle to be largely independent of laser intensity because

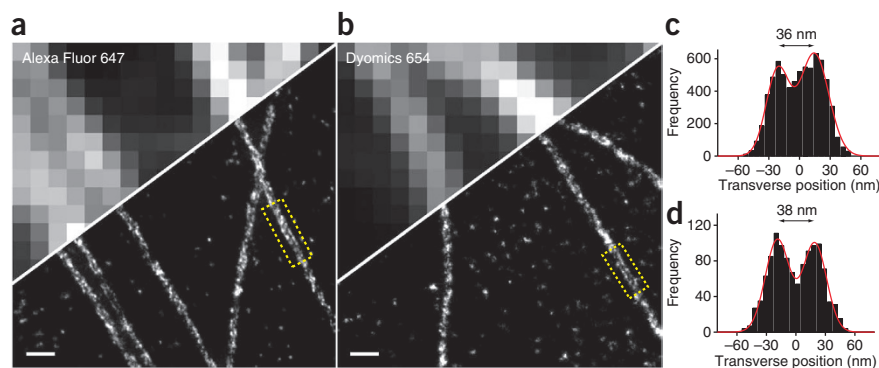


**Figure 3** | Alexa Fluor 647 and Dyomics 654 resolve the hollow structure of immunostained microtubules. **(a,b)** STORM images of microtubules immunostained with Alexa Fluor 647 **(a)** and Dyomics 654 **(b)** and partially overlaid conventional fluorescence images (top left). **(c,d)** Transverse profiles of localizations corresponding to regions boxed in yellow in **a** and **b**, respectively. Fitting of the profile by two Gaussian functions (red lines) gave the expected distances between the two peaks. Scale bars, 250 nm.

both the photon emission rate and off-switching rate tend to depend linearly on the excitation intensity (**Supplementary Fig. 32**). We observed some exceptions, such as the case of Cy3B where the number of photons per switching cycle increased with the excitation intensity (**Supplementary Fig. 32**). The equilibrium duty-cycle values also did not vary substantially with the laser intensity, as expected when both off- and on-switching rates depend linearly on the excitation intensity. In contrast, we observed a decrease in the survival fraction and the total number of switching cycles with increased excitation intensity for some dyes, such as Atto 655 (**Supplementary Fig. 32**). Therefore, whereas strong excitation intensity is often used to increase the switching rate and thus imaging speed, excessive laser intensity could reduce the image quality.

#### Summary of characterization for 26 dyes

In **Table 1** we summarize all four important properties that affect the STORM image quality, photon number, duty cycle, survival fraction and number of switching cycles. Details are available in **Supplementary Figures 2–27** for each of the 26 fluorophores, including dye structures (when available), fluorescence excitation and emission spectra, representative single-molecule fluorescence traces, photons per switching event, duty cycle, survival fraction as well as 2D STORM images of microtubules and CCPs. In **Table 2** we summarize the sensitivity of the dyes to activation by violet (405 nm) light, and in **Table 3** we summarize the on-off switching performance under different buffer conditions.

Overall, we observed large variability in the switching properties of the different dyes. The number of detected photons per switching event ranged from a few hundred to several thousand (**Table 1**). This wide range led to wide variability in the localization precision and hence STORM image resolution. We observed an even broader range of duty cycles, spanning two orders of magnitude (0.0001–0.04; **Table 1**). Although the duty cycle can be adjusted to some extent by changing buffer conditions, in particular by the use of different thiols<sup>12,39</sup>, for some dyes, the duty-cycle value is simply too high to obtain adequate image quality despite the broad range of conditions tested.

Accordingly, quality of STORM images afforded by these dyes also varied. Dyes with high photon numbers, low duty cycles, high survival fractions and many switching cycles in general performed well and resulted in high-quality images, whereas dyes with low photon numbers, high duty cycles, low survival fractions and/or few switching cycles did not (for example, fluorescein, FITC, Cy2, Cy3, Atto 565, Cy5.5, Atto 740, Alexa Fluor 790 and IRDye 800CW).

Several dyes in our screen had good overall properties, resulting in high-quality super-resolution images. Among these dyes, Alexa Fluor 647 (along with its structural analog Cy5) and Dyomics

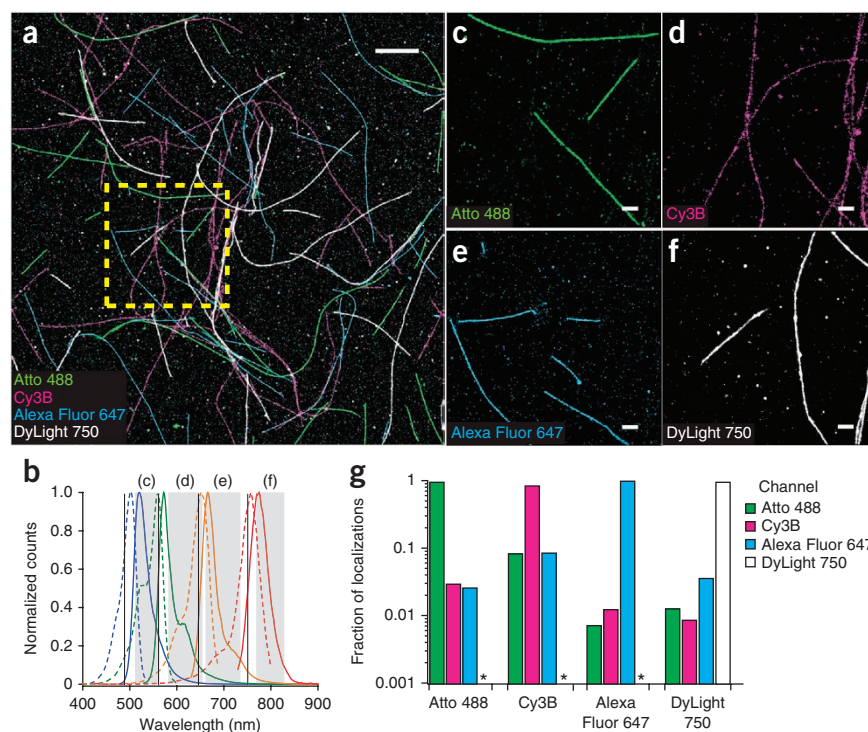


**Figure 4** | Four-color STORM imaging of *in vitro* assembled microtubule filaments and cross-talk analysis. **(a)** Four-color STORM image of *in vitro* assembled microtubules labeled with each of the four dyes, Atto 488 (green), Cy3B (magenta), Alexa Fluor 647 (cyan) and DyLight 750 (white). **(b)** Spectral separation of the four dyes, with the black vertical lines representing the excitation wavelength used and the gray regions highlighting the emission filter range for each of the dyes. **(c–f)** STORM images in each of the spectral regions for the boxed region in **a**. **(g)** Cross-talk between channels measured from control microtubule samples (undetectable in channels marked by an asterisk). Scale bars, 2  $\mu$ m **(a)** and 500 nm **(c–f)**.



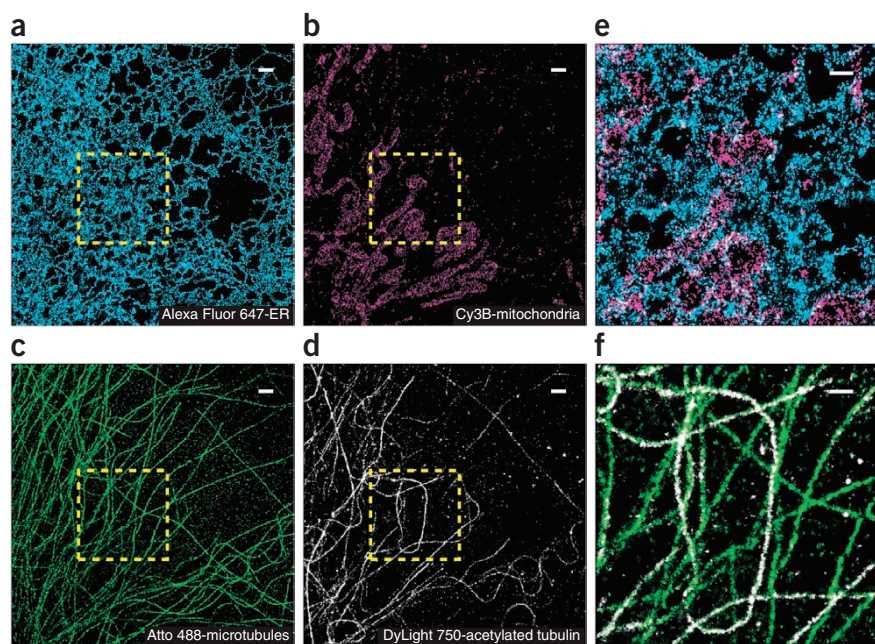


**Figure 5** | Four-color STORM imaging of cellular structures. (a–d) Individual channels of a four-color image of Alexa Fluor 647-labeled ER (cyan), Cy3B-labeled mitochondria (magenta), Atto 488-labeled microtubules (green) and DyLight 750-labeled acetylated tubulin (white) in a single fixed cell. (e) Magnification of the Cy3B and Alexa Fluor 647 channels of the boxed region in a–d showing extensive contact between mitochondria and the ER. (f) Magnification of the Atto 488 and DyLight 750 channels of the boxed regions in a–d showing overlap of acetylated tubulin with a subset of microtubule filaments. Scale bars, 1  $\mu$ m (a–d) and 500 nm (e,f).

654 emerged as top choices for their overall excellent properties. When we used Alexa Fluor 647 and Dyomics 654 to image microtubules, we could resolve the hollowness of immunostained microtubule filaments (Fig. 3). The transverse profile of localizations (Fig. 3c–d) showed two resolved peaks separated by 36–38 nm, as expected for the projection of a 25-nm-diameter cylinder that has been broadened by primary antibodies before staining with dye-labeled secondary antibodies.

### Multi-color STORM imaging with spectrally distinct dyes

From our screen we identified dyes with good performance in each of four distinct spectral ranges (blue, 480–540 nm, Atto 488; yellow, 545–600 nm, Cy3B; red, 640–700 nm, Alexa Fluor 647, Cy5 and Dyomics 654; and NIR, 740–805 nm, DyLight 750, Cy7 and Alexa Fluor 750) to demonstrate four-color STORM imaging. Several of these dyes (Atto 488, Dyomics 654, DyLight 750 and Cy7) were used for STORM imaging for the first time. The red dyes Alexa Fluor 647, Cy5 and Dyomics 654 performed considerably better than even the best-performing dyes in other spectral regions. In comparison, Atto 488, Cy3B, DyLight 750, Cy7 and Alexa Fluor 750 were substantially dimmer, and Cy3B additionally exhibited a lower number of switching cycles and a wider distribution of photons per switching cycle. Nevertheless, when compared to other dyes in each corresponding spectral band, these dyes exhibited the best overall performance in terms of photon output, duty cycle, survival fraction, number of switching cycles and quality of super-resolution images.

To perform four-color imaging, we first imaged a model sample of *in vitro*-prepared microtubules labeled with Atto 488, Cy3B, Alexa Fluor 647 (or Dyomics 654) and DyLight 750 (Fig. 4a and Supplementary Fig. 33a). We labeled the microtubules separately with each of these dyes and then mixed them before imaging. The excellent spectral separation afforded by the probes (Fig. 4b and Supplementary Fig. 33b) allowed us to achieve low cross-talk between the four channels (Fig. 4c–f and Supplementary Fig. 33c–f). We observed 0–3% cross-talk between different channels, except for Cy3B, which exhibited higher cross-talk

(~8%) into the Atto 488 and Alexa Fluor 647 (or Dyomics 654) channels (Fig. 4g and Supplementary Fig. 33g). Quantitative analysis of single, repetitively switching fluorophores allowed us to determine the resolution to be 29 nm for Atto 488, 22 nm for Cy3B, 17 nm for Alexa Fluor 647 (or Dyomics 654) and 30 nm for DyLight 750 (measured as the full-width at half-maximum of the localization distribution of individual probes; Supplementary Fig. 34). The variation corresponded well with photons per switching event for each dye.

Finally, we tested these probes in multicolor imaging of four different cellular targets. For this, we immunostained cells for tubulin, Tom20 (marker for mitochondrial outer membrane), ATL1 (marker for endoplasmic reticulum (ER)) and acetylated tubulin using Atto 488, Cy3B, Alexa Fluor 647 and DyLight 750, respectively. In Figure 5a–d we show STORM images for each of the four individual channels over the same field of view in a single cell. The excellent spectral separation allowed for easy color distinction of each cellular structure. In Figure 5e,f we show the magnified, overlaid images of the ER with mitochondria and microtubules with acetylated tubulin, respectively. In many instances, mitochondria nestled with extensive contacts with the ER network (Fig. 5e). As expected, only a subset of microtubules were acetylated (Fig. 5f). When replacing Alexa Fluor 647 with Dyomics 654 we obtained similar results (Supplementary Fig. 35).

### DISCUSSION

A key factor affecting the quality of STORM images is the choice of switchable probes. Here we showed that probe performance can be quantified in terms of the number of photons per switching event, the on-off duty cycle, the survival fraction when the probe reaches on-off equilibrium and the number of switching cycles. In general, fluorophores with high photon yield per switching event, low on-off duty cycle, high survival fraction and large number of switching cycles are desired for producing high-quality STORM images. Additional fluorophore parameters not included in this study may also be important, such as heterogeneity of switching properties across molecules (for example, variations in photon output or switching kinetics from molecule to molecule, which were appreciable for Cy3B) or compatibility with living cells. Another untested variable that may be pertinent is excitation wavelength. For example, Cy5.5 and IRDye 800CW, which showed the highest on-off duty cycles of all dyes tested, were evaluated using excitation



wavelengths (647 nm and 752 nm, respectively) that differed substantially (by ~30 nm) from their absorption peaks. Better matching of the excitation wavelength to the absorption maximum may help to minimize the duty cycle value, as we have observed for Alexa Fluor 647 (data not shown).

The choice of buffer composition is another important factor in achieving robust on-off switching of dyes. We tested two specific buffer additives, a primary thiol and an oxygen-scavenging system. For all dyes investigated, we obtained the best results with the imaging buffer containing both a primary thiol and an oxygen-scavenging system. Regardless of their structures, the dyes in our screen typically performed better in the presence of an oxygen-scavenging system. For some dyes (Atto 488, Alexa Fluor 488, Atto 520, Cy3B and Atto 680), we achieved on-off switching and reasonably good STORM performance even without a thiol. These observations suggest that a stable dark state could be achieved for these dyes by a thiol-independent pathway distinct from the previously suggested thiol-dependent formation of dark radical or reduced species<sup>45</sup>. In contrast, red and NIR-cyanine dyes, such as Alexa Fluor 647, require a thiol for robust switching, consistent with the previous finding that they form a covalent conjugate with the thiol in the dark state<sup>44</sup>. The concentration and identity of the thiol can also quantitatively impact the dye's switching properties and the STORM image quality. Non-thiol buffer additives such as ascorbic acid and methyl viologen can also be used to switch dyes<sup>16</sup>, although we did not explore the use of these buffer additives here. In general, investigation of the photochemical mechanisms underlying dark state formation is challenging owing to the presence of different types of dark states<sup>10,44–47</sup> and the fact that buffer components, such as thiol or dissolved oxygen, can have different roles (as reducing agents, triplet-state quenchers, radical scavengers and others). Studies to elucidate physical mechanisms of photoswitching should help rational design of optimal buffer conditions.

From this screen, we identified dyes suitable for STORM in each of four separate spectral bands (blue, yellow, red and NIR) and demonstrated four-color STORM imaging using these probes. This approach of using probes with minimal spectral overlap<sup>8</sup> gave lower cross-talk between color channels than multicolor approaches that use probes with the same emission color but different activation wavelengths (by pairing different activators with the same reporter)<sup>6</sup> or that use two-channel ratiometric detection of fluorophores with partially overlapping spectra<sup>48</sup>. We achieved the low cross-talk without sacrificing the density of molecules, as occurs when detecting two or more channels that overlap spectrally. In contrast, the use of different activation wavelengths<sup>6</sup> or ratiometric detection methods<sup>48</sup> also offers advantages over the multicolor imaging scheme used here. For instance, multiple activator-reporter pairs may be implemented using the best-performing dye (Alexa Fluor 647 or its close structural analogs), which performs far better than fluorophores in the other spectral channels, thus enabling multicolor super-resolution imaging with high resolution in all color channels<sup>6,12,41</sup>. Only one detection channel is required in this case, allowing automatic and perfect registration of the different color channels. Ratiometric detection of two or more spectrally overlapped fluorophores can be performed in principle with a single imaging laser and allows all fluorophores to be imaged simultaneously<sup>48</sup>. We note, however, that the spectrally distinct fluorophores used here may also be

imaged simultaneously using multichannel detection, although the intense short wavelength light used to image blue or yellow dyes could potentially over-activate the red or NIR dyes, and care should be taken when pursuing this strategy.

Here we only sampled a small subset of organic dyes and imaging buffer conditions, leaving open the possibility of even better probes and more optimal imaging conditions yet to be identified. In addition to organic dyes, a systematic and comparative study of photoswitchable fluorescent proteins<sup>23</sup> would also greatly benefit studies using super-resolution imaging. The criteria we established here may be used in the future to test probes not included in this analysis. A thorough understanding of the important probe properties will facilitate optimal probe selection for effective applications of super-resolution fluorescence microscopy.

## METHODS

Methods and any associated references are available in the online version of the paper at <http://www.nature.com/naturemethods/>.

*Note: Supplementary information is available on the Nature Methods website.*

## ACKNOWLEDGMENTS

We thank C. Blackstone (US National Institutes of Health) for the *myc-ATL1* construct. This work is supported in part by the US National Institutes of Health (to X.Z.). J.C.V. is supported in part by a Burroughs-Wellcome Career Award at the Scientific Interface. K.H.C. acknowledges a National Science Scholarship from the Agency for Science, Technology and Research of Singapore. X.Z. is funded by the Howard Hughes Medical Institute.

## AUTHOR CONTRIBUTIONS

G.T.D., J.C.V., K.H.C. and X.Z. designed the experiments. G.T.D., J.C.V., K.H.C. and M.B. performed the experiments. G.T.D., J.C.V. and K.H.C. performed the data analysis and interpretation. G.T.D., J.C.V. and X.Z. wrote the manuscript. X.Z. supervised the project.

## COMPETING FINANCIAL INTERESTS

The authors declare no competing financial interests.

Published online at <http://www.nature.com/naturemethods/>.

Reprints and permissions information is available online at <http://www.nature.com/reprints/index.html>.

- Hell, S.W. Far-field optical nanoscopy. *Science* **316**, 1153–1158 (2007).
- Huang, B., Babcock, H. & Zhuang, X. Breaking the diffraction barrier: super-resolution imaging of cells. *Cell* **143**, 1047–1058 (2010).
- Rust, M.J., Bates, M. & Zhuang, X. Sub-diffraction-limit imaging by stochastic optical reconstruction microscopy (STORM). *Nat. Methods* **3**, 793–795 (2006).
- Betzig, E. *et al.* Imaging intracellular fluorescent proteins at nanometer resolution. *Science* **313**, 1642–1645 (2006).
- Hess, S.T., Girirajan, T.P.K. & Mason, M.D. Ultra-high resolution imaging by fluorescence photoactivation localization microscopy. *Biophys. J.* **91**, 4258–4272 (2006).
- Bates, M., Huang, B., Dempsey, G.T. & Zhuang, X. Multicolor super-resolution imaging with photo-switchable fluorescent probes. *Science* **317**, 1749–1753 (2007).
- Folling, J. *et al.* Photochromic rhodamines provide nanoscopy with optical sectioning. *Angew. Chem. Int. Edn Engl.* **46**, 6266–6270 (2007).
- Bock, H. *et al.* Two-color far-field fluorescence nanoscopy based on photoswitchable emitters. *Appl. Phys. B* **88**, 161–165 (2007).
- Conley, N.R., Biteen, J.S. & Moerner, W.E. Cy3-Cy5 covalent heterodimers for single-molecule photoswitching. *J. Phys. Chem. B* **112**, 11878–11880 (2008).
- Folling, J. *et al.* Fluorescence nanoscopy by ground-state depletion and single-molecule return. *Nat. Methods* **5**, 943–945 (2008).
- Heilemann, M. *et al.* Subdiffraction-resolution fluorescence imaging with conventional fluorescent probes. *Angew. Chem. Int. Edn Engl.* **47**, 6172–6176 (2008).

12. Huang, B., Jones, S.A., Brandenburg, B. & Zhuang, X. Whole-cell 3D STORM reveals interactions between cellular structures with nanometer-scale resolution. *Nat. Methods* **5**, 1047–1052 (2008).
13. Flors, C., Ravarani, C.N. & Dryden, D.T. Super-resolution imaging of DNA labelled with intercalating dyes. *ChemPhysChem* **10**, 2201–2204 (2009).
14. Zhuang, X. Nano-imaging with STORM. *Nat. Photonics* **3**, 365–367 (2009).
15. Heilemann, M., van de Linde, S., Mukherjee, A. & Sauer, M. Super-resolution imaging with small organic fluorophores. *Angew. Chem. Int. Edn Engl.* **48**, 6903–6908 (2009).
16. Vogelsang, J., Cordes, T., Forthmann, C., Steinhauer, C. & Tinnefeld, P. Controlling the fluorescence of ordinary oxazine dyes for single-molecule switching and superresolution microscopy. *Proc. Natl. Acad. Sci. USA* **106**, 8107–8112 (2009).
17. Belov, V.N., Wurm, C.A., Boyarskiy, V.P., Jakobs, S. & Hell, S.W. Rhodamines NN: a novel class of caged fluorescent dyes. *Angew. Chem. Int. Edn Engl.* **49**, 3520–3523 (2010).
18. Lee, H.L. *et al.* Superresolution imaging of targeted proteins in fixed and living cells using photoactivatable organic fluorophores. *J. Am. Chem. Soc.* **132**, 15099–15101 (2010).
19. Scherwing, M. *et al.* Far-field nanoscopy with reversible chemical reactions. *Angew. Chem. Int. Edn Engl.* **50**, 2940–2945 (2011).
20. Jones, S.A., Shim, S.H., He, J. & Zhuang, X. Fast, three-dimensional super-resolution imaging of live cells. *Nat. Methods* **8**, 499–508 (2011).
21. Baddeley, D. *et al.* 4D super-resolution microscopy with conventional fluorophores and single wavelength excitation in optically thick cells and tissues. *PLoS ONE* **6**, e20645 (2011).
22. Fernandez-Suarez, M. & Ting, A.Y. Fluorescent probes for super-resolution imaging in living cells. *Nat. Rev. Mol. Cell Biol.* **9**, 929–943 (2008).
23. Patterson, G., Davidson, M., Manley, S. & Lippincott-Schwartz, J. Superresolution imaging using single-molecule localization. *Annu. Rev. Phys. Chem.* **61**, 345–367 (2010).
24. Hoyer, P., Staudt, T., Engelhardt, J. & Hell, S.W. Quantum dot blueing and blinking enables fluorescence nanoscopy. *Nano Lett.* **11**, 245–250 (2011).
25. Habuchi, S. *et al.* Reversible single-molecule photoswitching in the GFP-like fluorescent protein Dronpa. *Proc. Natl. Acad. Sci. USA* **102**, 9511–9516 (2005).
26. Brakemann, T. *et al.* A reversibly photoswitchable GFP-like protein with fluorescence excitation decoupled from switching. *Nat. Biotechnol.* **29**, 942–947 (2011).
27. Grotjohann, T. *et al.* Diffraction-unlimited all-optical imaging and writing with a photochromic GFP. *Nature* **478**, 204–208 (2011).
28. Patterson, G.H. & Lippincott-Schwartz, J. A photoactivatable GFP for selective photolabeling of proteins and cells. *Science* **297**, 1873–1877 (2002).
29. Subach, F.V. *et al.* Photoactivatable mCherry for high-resolution two-color fluorescence microscopy. *Nat. Methods* **6**, 153–159 (2009).
30. Chudakov, D.M. *et al.* Photoswitchable cyan fluorescent protein for protein tracking. *Nat. Biotechnol.* **22**, 1435–1439 (2004).
31. Wiedenmann, J. *et al.* EosFP, a fluorescent marker protein with UV-inducible green-to-red fluorescence conversion. *Proc. Natl. Acad. Sci. USA* **101**, 15905–15910 (2004).
32. McKinney, S.A., Murphy, C.S., Hazelwood, K.L., Davidson, M.W. & Looger, L.L. A bright and photostable photoconvertible fluorescent protein. *Nat. Methods* **6**, 131–133 (2009).
33. Gurskaya, N.G. *et al.* Engineering of a monomeric green-to-red photoactivatable fluorescent protein induced by blue light. *Nat. Biotechnol.* **24**, 461–465 (2006).
34. Sharonov, A. & Hochstrasser, R.M. Wide-field subdiffraction imaging by accumulated binding of diffusing probes. *Proc. Natl. Acad. Sci. USA* **103**, 18911–18916 (2006).
35. Bates, M., Huang, B. & Zhuang, X. Super-resolution microscopy by nanoscale localization of photo-switchable fluorescent probes. *Curr. Opin. Chem. Biol.* **12**, 505–514 (2008).
36. Thompson, R.E., Larson, D.R. & Webb, W.W. Precise nanometer localization analysis for individual fluorescent probes. *Biophys. J.* **82**, 2775–2783 (2002).
37. Yildiz, A. *et al.* Myosin V walks hand-over-hand: single fluorophore imaging with 1.5 nm localization. *Science* **300**, 2061–2065 (2003).
38. Shroff, H., Galbraith, C.G., Galbraith, J.A. & Betzig, E. Live-cell photoactivated localization microscopy of nanoscale adhesion dynamics. *Nat. Methods* **5**, 417–423 (2008).
39. van de Linde, S. *et al.* Direct stochastic optical reconstruction microscopy with standard fluorescent probes. *Nat. Protoc.* **6**, 991–1009 (2011).
40. Huang, B., Wang, W., Bates, M. & Zhuang, X. Three-dimensional super-resolution imaging by stochastic optical reconstruction microscopy. *Science* **319**, 810–813 (2008).
41. Dani, A., Huang, B., Bergan, J., Dulac, C. & Zhuang, X. Superresolution imaging of chemical synapses in the brain. *Neuron* **68**, 843–856 (2010).
42. Bates, M., Blosser, T.R. & Zhuang, X. Short-range spectroscopic ruler based on a single-molecule optical switch. *Phys. Rev. Lett.* **94**, 108101 (2005).
43. Heilemann, M., Margeat, E., Kasper, R., Sauer, M. & Tinnefeld, P. Carbocyanine dyes as efficient reversible single-molecule optical switch. *J. Am. Chem. Soc.* **127**, 3801–3806 (2005).
44. Dempsey, G.T. *et al.* Photoswitching mechanism of cyanine dyes. *J. Am. Chem. Soc.* **131**, 18192–18193 (2009).
45. van de Linde, S. *et al.* Photoinduced formation of reversible dye radicals and their impact on super-resolution imaging. *Photochem. Photobiol. Sci.* **10**, 499–506 (2011).
46. Steinhauer, C., Forthmann, C., Vogelsang, J. & Tinnefeld, P. Superresolution microscopy on the basis of engineered dark states. *J. Am. Chem. Soc.* **130**, 16840–16841 (2008).
47. Kottke, T., Van de Linde, S., Sauer, M., Kakorin, S. & Heilemann, M. Identification of the product of photoswitching of an oxazine fluorophore using Fourier transform infrared difference spectroscopy. *J. Phys. Chem. Lett.* **1**, 3156–3159 (2010).
48. Testa, I. *et al.* Multicolor fluorescence nanoscopy in fixed and living cells by exciting conventional fluorophores with a single wavelength. *Biophys. J.* **99**, 2686–2694 (2010).



## ONLINE METHODS

**Dyes and antibodies.** Dyes were obtained from Amersham (Cy2, Cy3, Cy3B, Cy3.5, Cy5, Cy5.5 and Cy7), Invitrogen (Alexa Fluors (here referred to as Alexa) 488, 568, 647, 750 and 790), ATTO-TEC (Atto 520, Atto 565, Atto 647, Atto 655, Atto 680 and Atto 740), Sigma (Atto 488 and Atto 647N), Anaspec (5(6)-TAMRA), Pierce (FITC, fluorescein and DyLight 750), Dyomics (Dyomics 654) and LI-COR (IRDye 800CW). All purchased dyes contained an N-hydroxysuccinimidyl ester (NHS) group for conjugation to protein, with the exception of FITC, which contains an isothiocyanate moiety for protein coupling. Primary antibodies were purchased from Abcam (mouse antibody to clathrin, ab2731; rat antibody to tubulin, ab6160; mouse antibody to acetylated tubulin, ab24610; goat antibody to myc, ab9132), and Santa Cruz Biotechnology (rabbit antibody to TOM20, sc-11415). Unconjugated secondary antibodies were purchased from Jackson ImmunoResearch Laboratories, including donkey anti-mouse (715-005-151), donkey anti-rat (712-005-153), donkey anti-rabbit (711-005-152) and bovine anti-goat (805-005-180).

**Fluorescence microscope.** All single-molecule and imaging measurements were performed on an Olympus IX-71 inverted microscope configured for either total internal reflection fluorescence (TIRF) or oblique incidence excitation. In the oblique incidence geometry, the incidence angle was slightly below the critical angle such that the excitation light illuminated 1–2  $\mu\text{m}$  deep into the sample in the field of view. The samples were continuously illuminated using different excitation sources depending on the fluorophore used. Blue- and red-absorbing dyes were excited using the 488 nm and 647 nm lines of a mixed-gas argon-krypton laser (Innova 70C; Coherent), respectively; yellow-absorbing dyes were excited with a 561-nm diode-pumped solid-state laser (Sapphire 561; Coherent); NIR-absorbing dyes were excited using the 752-nm line of a krypton laser (Innova 302C; Coherent). A 405-nm solid-state laser (Cube 405-100C; Coherent) was used for activation of dyes as described below. Beam selection and modulation of the laser intensities were controlled in several ways, depending on the laser wavelength. For 488-nm and 647-nm lines, an acousto-optic tunable filter (AA Optoelectronic) was used. The 561-nm and 752-nm lines were controlled using mechanical shutters (Uniblitz). For the 405-nm line, the light was controlled by direct digital modulation of the laser power supply. In all cases, neutral density filter wheels were used for coarse adjustments of laser power along with a combination of a half-wave plate and polarizer for fine power adjustments.

The following longpass dichroic mirrors were used to reflect the excitation sources listed above: T495LP (Chroma) for 488 nm, Di01-R561 (Semrock) for 561 nm, Z660DCXRU (Chroma) for 647 nm and Q770DCXR (Chroma) for 752 nm. Fluorescence was collected using an Olympus UPlanSApo 100 $\times$ , 1.4 numerical aperture (NA) oil-immersion objective lens and passed through either one of the following bandpass emission filters: 535/50 (ET535/50m; Chroma) for blue-absorbing dyes; 617/73 (FF01-617/73-25; Semrock) for yellow-absorbing dyes; 700/75 (ET700/75m; Chroma) for red-absorbing dyes; or 800/60 (HQ800/60m; Chroma) for NIR-absorbing dyes. All movies were recorded onto a 256  $\times$  256 pixel region of an electron-multiplying charge coupled device (EMCCD) camera (iXon 897; Andor).

During data acquisition, a home-built focus lock was used to maintain a constant focal plane as described previously<sup>49</sup>.

Briefly, a 975-nm infrared laser diode (PL980P330J; Thorlabs) was directed toward the sample using a dichroic mirror (900DCSP; Chroma). The beam reflected off of the sample was detected by a quadrant photodiode (QPD). Changes in the axial position of the sample resulted in a shift of the reflected beam position on the QPD. A feedback system using custom LabVIEW software then adjusted the sample z-dimension position using a piezo stage (NZ100CE; Prior Scientific) until the original beam position was restored.

**Imaging buffers.** Detailed single-molecule characterization and STORM imaging for each dye (Figs. 2–5, Tables 1–3 and Supplementary Figs. 1–35) was performed in an imaging buffer that contained TN buffer (50 mM Tris (pH 8.0) and 10 mM NaCl), an oxygen scavenging system (0.5 mg ml<sup>−1</sup> glucose oxidase (Sigma-Aldrich), 40  $\mu\text{g}$  ml<sup>−1</sup> catalase (Roche or Sigma-Aldrich) and 10% (w/v) glucose) and either 143 mM  $\beta$ ME or 10 mM MEA (Fluka), unless otherwise indicated. MEA was stored as a solid at 4 °C and prepared fresh as a 1 M stock solution in water with pH adjusted to ~8 with 1 M aqueous KOH. This stock solution was kept at 4 °C and used within 1–2 weeks of preparation.  $\beta$ ME was stored as a neat liquid (14.3 M) at 4 °C. For experiments, the thiol solutions were diluted immediately before imaging to the final concentrations as described above.

Buffer-dependence experiments (Supplementary Figs. 29–30 and Table 3) were performed using one of the following four different buffers: PBS only (‘no GLOX or thiol’ condition), TN buffer with 10 mM MEA (‘thiol only’ condition), TN buffer with oxygen scavenger with the above described composition (‘GLOX only’ condition), and TN buffer with 10 mM MEA and oxygen scavenger with the above described composition (‘GLOX and thiol’ condition). To assess whether any free thiol was present in the ‘GLOX only’ solution, we measured the absorption increase at ~410 nm of the ‘GLOX only’ buffer upon addition of 50  $\mu\text{M}$  Ellman’s reagent (5,5′-dithiobis(2-nitrobenzoic acid); Sigma-Aldrich), a standard assay for free thiol quantification<sup>50</sup>. No absorption increase was detectable. In contrast, absorption increase was observed for a series of standard 1–20  $\mu\text{M}$  cysteine solutions. This measurement placed an upper limit of the thiol concentration of our ‘GLOX only’ buffer to <1  $\mu\text{M}$ .

**Single-molecule sample preparation.** Single-molecule characterization of fluorophores was performed using dye-labeled donkey anti-rat secondary antibodies. Antibodies were labeled using the manufacturers’ protocols. In brief, 10  $\mu\text{l}$  of 1 M aqueous NaHCO<sub>3</sub> (pH 8.0) was added to 50–100  $\mu\text{g}$  of antibody to a final antibody concentration of ~2  $\mu\text{M}$ . Dyes were dissolved in dimethyl sulfoxide and added to antibody solutions at varying dye concentrations (typically at a final concentration of ~4  $\mu\text{M}$  to achieve the desired dye to protein ratios). Dyes could be stored for long term as a solid at −20 °C. Labeled antibodies were purified by gel filtration using NAP-5 columns (GE Healthcare). The labeling ratio was determined using a Beckman-Coulter UV-Vis spectrophotometer. All dye-labeled antibodies for single-molecule characterization measurements had dye-labeling ratios 0.2–0.8 dyes per antibody such that the majority of dye-labeled antibody molecules were labeled with only one dye molecule. Labeled antibodies were immobilized on the surface of a flow chamber assembled from a glass slide and a number 1.5 coverslip



that were separated by double-sided tape. Slides and coverslips were cleaned by sonication for 15 min in each of the following: Alconox solution, followed by Mili-Q water, followed by 100% ethanol and last 1 M aqueous potassium hydroxide. Coverslips were then washed with Mili-Q water and blow-dried with compressed nitrogen before assembly of the flow chamber. The labeled antibodies were adsorbed to the coverslip at a low density (typically  $0.04\text{--}0.12\text{ dye }\mu\text{m}^{-2}$ ) such that individual dye molecules could be clearly resolved from each other. Control experiments showed that labeled antibodies did not detach from the surface on the time scale of the experiments (data not shown). The flow chambers were rinsed extensively with PBS to remove unbound antibodies before imaging.

**Single-molecule fluorescence measurements.** Blue-, yellow-, red- and NIR-absorbing dyes were illuminated with 488-nm ( $1.2\text{ kW cm}^{-2}$ ), 561-nm ( $2.2\text{ kW cm}^{-2}$ ), 647-nm ( $0.8\text{ kW cm}^{-2}$ ) or 752-nm ( $1.3\text{ kW cm}^{-2}$ ) laser light in a total-internal reflection geometry. Under constant illumination and the buffer conditions described above, the dyes typically started in the fluorescent state, switched to a dark state and spontaneously recovered to a fluorescent state multiple times before photobleaching. For each dye, several movies of 1,500–2,000 s duration were recorded, and 50–150 single-molecule fluorescence time traces were obtained per movie. All movies were collected at a frame rate of 33 Hz. Control samples lacking fluorescently labeled antibodies, but otherwise prepared in the same way, yielded virtually no detected fluorescent molecules in each of the four spectral ranges studied (data not shown). The low density of adsorbed fluorescent antibodies ( $<0.1\text{ }\mu\text{m}^{-2}$ ) and the low number of dyes per antibody molecule ( $<0.8$  per antibody) were chosen to minimize the probability that fluorescent signals being studied originated from more than one dye molecule. Additional control experiments were performed to assess what fraction of fluorescent signals originated from single fluorophores by imaging adsorbed dye-labeled antibodies under buffer conditions that have been previously shown to drastically reduce fluorophore blinking (TN buffer with GLOX and 1 mM trolox)<sup>51</sup>. These experiments revealed that  $>90\%$  of fluorescent spots showed single-step photobleaching, ensuring single-molecule detection under our imaging conditions.

**Single-molecule data analysis.** In the initial frame of each single-molecule-characterization movie, the positions of adsorbed molecules were determined by identifying fluorescent signals above a threshold of 4 times the s.d. of the fluctuations of the detected background signal. Any fluorescent molecule within five pixels (peak to peak separation, with 160 nm per pixel) of another fluorescent molecule was omitted from analysis. Fluorescence time traces were calculated for each molecule by analyzing the total integrated signal in a  $7\times 7$  pixel region centered on the molecule during each frame of the movie. The number of photons detected per switching event was calculated as the total integrated signal minus the background intensity counts, which was converted to photons using the calibrated curve for the electron multiplication and analog-to-digital conversion gain settings used during acquisition. Fluorescence switching events were identified within the time traces by identifying signal changes with a magnitude that is greater than 5–10 times the s.d. of the background fluctuations

of the fluorescence time trace. The on-off duty cycle,  $DC$ , of the dyes was calculated within a sliding window of 100 s as

$$DC = \left\langle \frac{\sum_i \tau_{\text{on},i}}{100\text{s}} \right\rangle$$

where  $\tau_{\text{on},i}$  denotes the on-time of the  $i^{\text{th}}$  switching event for a given molecule within the time window, and the brackets indicate averaging over all molecules not yet photobleached. The equilibrium duty cycle reported was the mean of the duty cycle value between 400–600 s. Photobleached molecules were not included in the duty cycle calculation for times past photobleaching. Note that we only report the duty cycle and survival fraction, that is, the fraction of dyes not yet photobleached, for the first 700 s of illumination although the total movie was 2,000 s long. Therefore, only molecules that photobleached within the first 700 s need to be identified. Here we consider a molecule to be bleached after the final on event identified for that molecule in the movie. The molecules that were identified to be bleached during the first 700 s based on this criterion most likely have in fact been photobleached given that the remaining 1,300 s of the movie is typically 4–20 times longer in duration than the mean off time of each fluorophore.

To measure dye sensitivity to activation by violet light, samples were first illuminated for 1,500 frames at 20 Hz frame rate at their respective excitation wavelength (488 nm, 561 nm, 647 nm or 752 nm) to switch most dyes into a dark state. After this, the imaging laser was turned off and a 0.25-s, 405-nm laser pulse ( $10\text{--}30\text{ W cm}^{-2}$ ) was applied. The samples were then immediately illuminated with the imaging lasers again. The number of molecules that recovered was counted and compared with the original number of molecules present at the beginning to give the recovery fraction. The recovery fraction values reported were corrected for non-violet-induced blinking by subtracting the average number of molecules per frame in the 100 frames preceding the application of the 405 nm laser pulse.

**Immunofluorescence staining of cellular structures.** Immunostaining was performed using BS-C-1 cells (American Type Culture Collection) cultured with Eagle's Minimum Essential Medium fortified with 10% FBS, penicillin and streptomycin, and incubated at  $37^\circ\text{C}$  with 5%  $\text{CO}_2$ . Cells were plated in LabTek 8-well coverglass chambers (Nunc) at  $\sim 20,000$  cells per well on the day before fixation.

The immunostaining procedure for clathrin consisted of: fixation for 20 min with 4% paraformaldehyde (Electron Microscopy Sciences) in PBS, washing with PBS, permeabilization for 2 min with 0.5% Triton X-100 and 3% bovine serum albumin (BSA; Jackson ImmunoResearch Laboratories) in PBS, blocking for 60 min with 0.2% Triton X-100 and 3% BSA in PBS (blocking buffer 1), incubation for 60 min with mouse anti-clathrin heavy chain monoclonal antibody diluted to  $2\text{ }\mu\text{g ml}^{-1}$  in blocking buffer 1, washing with blocking buffer 1, incubation for 30 min with dye-labeled donkey anti-mouse secondary antibody ( $\sim 1\text{--}2$  dyes per antibody) at a concentration of  $\sim 2.5\text{ }\mu\text{g ml}^{-1}$  in blocking buffer 1, washing with blocking buffer 1; washing with PBS, fixation after labeling for 10 min with 3% paraformaldehyde and 0.1% glutaraldehyde (Electron Microscopy Sciences) in PBS and finally washing with PBS.

The immunostaining procedure for microtubules consisted of fixation for 10 min with 3% paraformaldehyde and 0.1% glutaraldehyde in PBS, washing with PBS, reduction for 5 min with 0.1% sodium borohydride in PBS to reduce background fluorescence, washing with PBS, blocking for 30 min with 3% bovine serum albumin and 0.25% (v/v) Triton X-100 in PBS (blocking buffer 2), staining for 45 min with primary antibody to tubulin (rat anti-tubulin) diluted in blocking buffer 2 to a concentration of  $10\ \mu\text{g ml}^{-1}$ , washing with PBS, incubation for 45 min with secondary antibodies ( $\sim 1\text{--}2$  dyes per antibody) at a concentration of  $\sim 2.5\ \mu\text{g ml}^{-1}$  in blocking buffer 2, washing with PBS, fixation after labeling for 10 min with 3% paraformaldehyde and 0.1% glutaraldehyde in PBS, and finally washing with PBS.

The procedure for multicolor immunostaining of tubulin, acetylated tubulin, endoplasmic reticulum and mitochondria was nearly identical to the microtubule immunostaining protocol described above except for the following nucleofection procedures, antibody concentrations and dye labeling ratios. Before seeding, cells were nucleofected with a plasmid encoding myc-ATL1 (gift of C. Blackstone<sup>52</sup>) using an Amaxa Nucleofector II (Lonza) with Amaxa Cell Line Nucleofector Kit V (Lonza)  $\sim 24$  h before fixation. Primary antibodies were used at concentrations of  $\sim 10\ \mu\text{g ml}^{-1}$  (rat anti-tubulin, goat anti-myc),  $\sim 20\ \mu\text{g ml}^{-1}$  (mouse anti-acetylated tubulin) and  $\sim 2\ \mu\text{g ml}^{-1}$  (rabbit anti-TOM20) in blocking buffer 2. Secondary antibodies were labeled at a dye-to-protein ratio of  $\sim 2.6$  Atto 488 dyes per donkey anti-rat antibody,  $\sim 1.7$  DyLight 750 dyes per donkey anti-mouse antibody,  $\sim 1.5$  Alexa 647 (or  $\sim 1.7$  Dyomics 654) dyes per bovine anti-goat antibody and  $\sim 3.1$  Cy3B dyes per donkey anti-rabbit antibody.

***In vitro* assembled microtubules.** Microtubules were grown and labeled according to the following protocol. Two prechilled 1 mg tubulin aliquots (T240; Cytoskeleton) were carefully dissolved in a total of 500  $\mu\text{l}$  of a prechilled solution consisting of PEM (100 mM PIPES (pH 7.0), 1 mM EGTA and 1 mM  $\text{MgCl}_2$ ) with 1 mM GTP (BST06; Cytoskeleton) and 10% glycerol (v/v). After centrifugation for 10 min at 18,000g at 4 °C, the supernatant was incubated at 37 °C for 20 min to polymerize the microtubules. The microtubules were then stabilized by addition of paclitaxel (TXD01; Cytoskeleton) to 1 mM and incubation for 5 min at 37 °C, and then stored at 25 °C. Polymerized microtubules were labeled with dye by incubation of 60  $\mu\text{l}$  of  $\sim 4\ \text{mg ml}^{-1}$  polymerized microtubules with either 0.13 mM Atto488-NHS, 0.16 mM Cy3B-NHS, 0.77 mM Alexa 647-NHS, 0.45 mM Dyomics 654-NHS or 0.64 mM DyLight 750-NHS for 60 min. Dye-labeled microtubules were purified from free dye by centrifugation through a dense layer consisting of PEM with 60% (v/v) glycerol and 1 mM paclitaxel for 2 h at 300,000g. Labeled microtubule pellets were washed carefully and then gently resuspended in 50  $\mu\text{l}$  of buffer consisting of PEM with 1 mM paclitaxel. Four single-color-labeled microtubule samples was mixed (either Atto 488, Cy3B, Alexa 647 and DyLight 750 or Atto 488, Cy3B, Dyomics 654 and DyLight 750), diluted 1:10 in PEM with 1 mM paclitaxel, and incubated for 10 min in LabTek 8-well chambers which had been cleaned by sonication in 1 M aqueous potassium hydroxide and silanized by incubation with 1% N-(2-aminoethyl)-3-aminopropyl trimethoxysilane (UCT Specialties), 5% acetic acid and 94% methanol for 20 min to facilitate microtubule adsorption to coverglass. The immobilized microtubules were

fixed by incubation for 10 min with 0.5% glutaraldehyde in PEM with 1 mM paclitaxel followed by washing with PEM.

**STORM imaging of immunostained cells and *in vitro* microtubules.** STORM imaging of immunostained cells was performed using one of five different buffer conditions described above. Samples were illuminated with oblique incidence and detected using different excitation sources, dichroic mirrors and emission filters depending on the fluorophore, as described above. For 3D STORM imaging, a 1-m cylindrical lens was inserted into the detection path to introduce astigmatism such that the images from individual molecules typically appeared elliptical. The  $x$ - $y$  and  $z$  positions of the molecules were determined from the centroid position and the ellipticity of the image, respectively, as previously described<sup>40</sup>. To determine the  $z$  position of the molecule from the ellipticity of the single-molecule image, a calibration curve of the change in ellipticity for different  $z$  positions is needed. The calibration curve was determined before imaging by recording fluorescence from single immobilized beads (580/605 nm, 200 nm diameter microspheres; Molecular Probes) while scanning the  $z$ -piezo stage over an 800-nm range (400 nm above and below the central focal plane where the molecule images are circular rather than elliptical).

All STORM movies for blue-, yellow- and red-absorbing dyes were collected at a frame rate of 61 Hz and those for NIR-absorbing dyes were collected at 33 Hz. An illumination intensity of  $1\text{--}3\ \text{kW cm}^{-2}$  was used for these movies. Under this imaging condition, all dye molecules are typically in the fluorescent state initially but rapidly switch to a dark state. Recording of STORM movies was started once a low density of fluorescent molecules was attained (after  $\sim 10\text{--}300$  s illumination) such that the images from individual fluorescence molecules were largely not overlapped with each other. All movie durations were 30,000–80,000 frames and were collected using constant illumination at the corresponding excitation wavelength for the dye. For fluorophores that were sensitive to activation with violet light (Table 2), we used continuous-wave 405-nm laser light ( $0.1\text{--}30\ \text{W cm}^{-2}$ , gradually increased during the movie to illuminate the sample to maintain a convenient density of activated molecules).

For multicolor imaging, dyes were imaged sequentially: DyLight 750, then Alexa 647 (or Dyomics 654), then Cy3B and Atto 488 last. Filters were switched between datasets for each color. About 70,000 frames were recorded in each color channel before switching to another channel. Simultaneous imaging of differently colored probes is in principle possible by properly separating the fluorescence emissions in the different color channels. However, owing to substantial activation of the red and NIR dyes by the blue light used to image Atto 488, the imaging quality may be compromised if all four color ranges were to be imaged simultaneously. For alignment between different color channels, bright-field images of 250 nm Au beads (Corpuscular) were taken before each STORM movie and used to register each channel into a common reference frame. We determined that the alignment error was  $<20$  nm, based on control experiments performed with beads that emit in all four spectral bands (data not shown).

**STORM image analysis and rendering.** STORM movies were analyzed as described previously using custom-written software in IDL and C++ (refs. 6,40). Briefly, individual frames were convolved with a zero-sum Gaussian to suppress image noise. Fluorescence peaks

corresponding to individual molecules were identified in each frame and fit using least-squares fitting with either a two-dimensional rotating cylindrical or elliptical Gaussian to determine the  $(x, y)$  position of each molecule. Maximum-likelihood estimator fitting of fluorophore positions could also be used<sup>53,54</sup>. For 3D imaging, the ellipticity of the Gaussian was used to assign a  $z$  coordinate as described previously<sup>40</sup>. Briefly, single-molecule images were fit to an elliptical Gaussian to obtain the centroid position coordinates ( $x$  and  $y$ ) and the Gaussian widths ( $dx$  and  $dy$ ). The  $z$  position was calculated from  $dx$  and  $dy$  using a calibration curve independently determined by scanning bead samples along the  $z$ -direction as described above. Each bead image was also fit to an elliptical Gaussian to obtain the Gaussian widths,  $dx$  and  $dy$ , and the average  $dx$  and  $dy$  values from many beads at different  $z$  positions were used to create the calibration curve. Molecules that were within a distance of 160 nm (one pixel) in successive frames were linked together and the mean position of the molecule in successive frames was used to report the position of that molecule.

Lateral and axial drift in the sample during acquisition was corrected computationally using image correlation as described previously<sup>6</sup>. Briefly, the STORM movie was segmented into non-overlapping, 2,000–4,000-frame segments, and the STORM image reconstructed from each segment was correlated to the first one in the series to monitor sample drift. This approach relies on maintaining a sufficient density of localizations from each set of frames to ensure the accuracy of the correlation. As mentioned above, STORM movies were taken using 405-nm activation with gradually increasing intensity to maintain this density. However, in the case of imaging a low-copy-number structure or imaging a moving sample<sup>20</sup>, fiducial markers, such as fluorescent or gold beads, should be used to track sample drift.

Finally, STORM images were rendered with each localization plotted as a Gaussian whose width is weighted by the inverse square root of the number of detected photons for that switching event. Images were filtered to reject molecules that are too dim (<300 photons), too elliptical ( $x$  and  $y$  axial ratio >1.5 for 2D images) or that are 'on' for >8 consecutive frames. Additional details on data analysis can be found elsewhere<sup>49,55</sup>.

Cellular autofluorescence and nonspecifically bound antibodies can give background in the STORM images, which appears as scattered localizations at low local densities. This background noise was removed in the four-color immunofluorescence images by a local density filter. Low-density localizations were filtered out by removing a localization if it was surrounded by fewer than 1–3 localizations in the 60 nm × 60 nm region surrounding the localization.

**Radial density analysis of clathrin-coated pits.** To determine the radial density of localizations for clathrin-coated pits (CCPs), the STORM images of ten CCPs were selected for each dye (Alexa

647, Atto 655 and Cy5.5) and a 40-nm-thick  $x$ – $y$  cross-section was taken at the midplane for each CCP. The cross-section images were then merged by aligning the center of mass for each pit to a common point. The localization density was calculated by determining the radial distance of each localization relative to the alignment point. The localizations were then binned and normalized by the area of each radial slice.

**Cross-talk analysis.** To determine cross-talk between spectral channels (Fig. 4g and Supplementary Fig. 34g), we obtained super-resolution images of *in vitro*-assembled microtubules labeled with one of the four probes in each of the four channels. For example, to determine the cross-talk of Alexa 647 into other channels, we imaged microtubules labeled with Alexa 647 in the DyLight 750 channel, followed by the Alexa 647 channel, the Cy3B channel and lastly the Atto 488 channel, the same imaging sequence as used in our actual imaging experiments. The percent of localizations contributing to the cross-talk was then determined from the STORM image in the DyLight 750, Cy3B and Atto 488 channels relative to the correct Alexa 647 channel. This procedure was repeated for each of the dyes used in multicolor imaging. We note that in the cross-talk measurements, each dye was imaged for ~40,000 frames in each channel. Imaging for ~40,000 frames in the correct channel (for example imaging Alexa 647 in the red channel) cause partial bleaching of the dyes, which could reduce the apparent cross-talk into the bluer channels imaged later in the sequence. However, because our four-color imaging experiments (Figs. 4a and 5 and Supplementary Figs. 33a and 35) used exactly the same red-to-blue imaging sequence but with a larger number of frames (~70,000 frames) per channel, which could lead to a larger extent of photobleaching than the cross-talk analysis experiments, we anticipate that the above cross-talk analysis actually overestimates the real cross-talk present in our four-color images.

49. Dempsey, G.T., Wang, W. & Zhuang, X. Fluorescence imaging at sub-diffraction limit resolution with stochastic optical reconstruction microscopy. in *Handbook of Single-molecule Biophysics* (eds. P. Hinterdorfer, van Oijen, A.M.) 95–127 (Springer Science and Business Media, 2009).
50. Riddles, P.W., Blakeley, R.L. & Zerner, B. Reassessment of Ellman's reagent. *Methods Enzymol.* **91**, 49–60 (1983).
51. Rasnik, I., McKinney, S.A. & Ha, T. Nonblinking and longlasting single-molecule fluorescence imaging. *Nat. Methods* **3**, 891–893 (2006).
52. Zhu, P.P. *et al.* Cellular localization, oligomerization, and membrane association of the hereditary spastic paraplegia 3A (SPG3A) protein atlastin. *J. Biol. Chem.* **278**, 49063–49071 (2003).
53. Mortensen, K.I., Churchman, L.S., Spudich, J.A. & Flyvbjerg, H. Optimized localization analysis for single-molecule tracking and super-resolution microscopy. *Nat. Methods* **7**, 377–381 (2010).
54. Laurence, T.A. & Chromy, B.A. Efficient maximum likelihood estimator fitting of histograms. *Nat. Methods* **7**, 338–339 (2010).
55. Bates, M., Jones, S. & Zhuang, X. Stochastic optical reconstruction microscopy (STORM)—a method for superresolution fluorescence imaging. in *Imaging: A Laboratory Manual* (ed. R. Yuste) 547–576 (Cold Spring Harbor Laboratory Press, 2011).